

THE USE OF FOURIER TRANSFORMS FOR ASYNOPTIC MAPPING: APPLICATIONS TO
THE UPPER ATMOSPHERE RESEARCH SATELLITE MICROWAVE LIMB SOUNDER

Lee S. Elson and Lucien Froidevaux

Jet Propulsion Laboratory, California Institute of Technology,
Pasadena, CA. 91109

Fourier analysis has been applied to data obtained from limb viewing instruments on the Upper Atmosphere Research Satellite. A coordinate system rotation facilitates the efficient computation of Fourier transforms in the temporal and longitudinal domains. Fields such as ozone (O_3), chlorine monoxide (ClO), temperature and water vapor have been transformed by this process. The transforms have been inverted to provide maps of these quantities at selected times, providing a method of accurate time interpolation. Maps obtained by this process show evidence of both horizontal and vertical transport of important trace species such as O_3 and ClO . An examination of the polar regions indicates that large scale planetary variations are likely to play a significant role in transporting mid-stratospheric O_3 into the polar regions. There is also evidence that downward transport occurs providing a means of moving O_3 into the polar vortex at lower altitudes. The transforms themselves show the structure and propagation characteristics of wave variations.

1. INTRODUCTION

The orbit of the Upper Atmosphere Research Satellite (UARS) {*Reber* (1990)}, launched on Sept. 12, 1991, is such that atmospheric emission measurements progress through all local solar times in about 36 days. In order for side-looking instruments to cover the high latitudes of both hemispheres, UARS performs a 180° yaw maneuver after covering all local times and the period between yaws is referred to as a UARS “month”. The emission instruments view all longitudes on a daily basis although the latitude sampling depends on the UARS yaw state.

Several higher order data products are routinely generated from emission observations. Level 3A data are profiles (on pressure surfaces) along the orbit track with equal temporal spacing (65 seconds) but unequal latitude and longitude spacing. Level 3B data, produced using a Kalman filter approach, are daily Fourier coefficients in longitude at 4° latitude intervals for each pressure surface. As described by *Haggard et al., (1986)* the Kalman filter technique uses statistics and sequential estimation. Among its advantages are its formal description of errors in the form of an error covariance matrix and its estimates for missing data. Kalman filtering, however, makes no attempt to account for the interdependence of longitude and time that arises because the observations were made by an orbiting instrument.

Another approach, which also uses Fourier analysis, has been developed by *Salby (1982a, 1982b)* and applied by *Lait and Stanford (1988)* and others. This approach expresses longitude and time variations in terms of Fourier transforms, which are functions of wavenumber, m and frequency σ . Inverse transforms can then be used to specify fields at one time thereby converting global observations acquired at different times (i.e. asynchronously) to synoptic maps. We therefore use the term “a synoptic mapping” to

describe this procedure. The implementation followed here differs from the above descriptions because of an emphasis on maps which contain all resolvable spectral contributions, because of the viewing geometry of the emission instruments and because of differences in several of the formulas which are used. Details of the approach are given in Section 2 and the Appendix.

Once a particular sampling pattern is known, the asynoptic mapping procedure can be tested by sampling a known field. Here we use the output from a general circulation model (GCM) sampled as the Microwave Limb Sounder (MLS) samples the atmosphere. Comparison of synoptic maps with the original GCM output, discussed in Section 3, provides insight into the capabilities and limitations of the approach.

Several data products result from the procedure outlined above. Synoptic maps can be reconstructed for any time during the observation period and can be compared with other data products such as conventional synoptic maps from the National Meteorological Center (NMC). Time sequences of maps show the evolution of a field. This approach makes possible a qualitative estimate of the horizontal and vertical transport of measured quantities. Selected sequences illustrating the evolution of both the Southern Hemisphere (SH) and Northern Hemisphere (NH) polar vortices are shown in Section 4.

Asynoptic mapping is also well suited for examining the latitude/height distribution of a disturbance at a particular m and σ since Fourier coefficients are its primary product. Section 4 gives examples of a large disturbance in the ozone (O_3) and temperature fields examined in this way.

2. ASYNOPTIC MAPPING OF MLS DATA

As discussed by Salby (1982a) asynoptic mapping expresses the longitude and time (A

and t) variations of a field in terms of its Fourier transforms. This would be quite simple if the λ and t values of the observations were orthogonal, i.e. if for each time, there were a series of observations made at many longitudes. Such is not the case for UARS, since it takes about 24 hours for the satellite to progress through 360° of longitude. By rotating the λ and t coordinates through an angle which depends on the longitudinal speed of the satellite, orthogonal independent variables are defined which correspond to λ and t . This rotation allows the application of conventional techniques, such as the Fast Fourier Transform (FFT). A rotation back to the original coordinate system permits these transforms to be expressed in the traditional way, enabling the use of inverse transforms to represent the observed field in real (A , t) space. The number and spacing of observations completely determine the range of allowable frequencies and their resolution or bandwidth. The spectral resolution, or spacing between frequencies, is given approximately by $2 \frac{\pi}{d}$ where d is the number of days of data in the series.

Several practical considerations must be considered. As discussed by *Lait and Stanford* (1988), missing or bad data must be filled since the FFT cannot proceed when data gaps are present. The work described here follows their approach by interpolating fewer than 10 missing data values along the orbit using data before and after the gap. Longer gaps are filled by interpolating between available orbits for a given latitude bin.

Another problem (*Salby*, 1982a) is that the ascending and descending series must be independent of each other. This is true except near the turning points of the orbits where the spatial and temporal separations of the series decrease to zero. This lack of independence can affect the results by introducing spurious variations within about 5° of the turning point. This occasionally occurs poleward of about $\pm 75^\circ$ latitude.

The FFT approach requires equal sampling intervals in space and time. Because the satellite executes a yaw maneuver periodically, this requirement is not satisfied for fixed view instruments for periods longer than a UARS month. This means that, for example,

even though the equatorial region (i-30°) is viewed continuously, it is not easy to construct a long term (greater than 1 UARS month), equally spaced time series for this region. Therefore the limit to the frequency resolution which can be obtained is about $\frac{2\pi}{36} \text{ rad day}^{-1}$ for a 36 day UARS month. An additional complication results from the fact that some instruments, such as the Improved Stratosphere and Mesosphere Sounder (ISAMS), are able to alter their sampling pattern. Although this provides great flexibility in observing different parts of the atmosphere, it can make the FFT difficult to calculate. It must be emphasized that this problem is a result of the FFT calculation and is not inherent in the coordinate system rotation. It is possible, for example, to use other techniques to calculate the Fourier transform at the expense of computational efficiency.

A potentially more serious difficulty can arise due to aliasing. This problem, if present, is dependent on the observing pattern and the signals present in the atmosphere, so it is inherent in any analysis of the data including the Kalman filter technique. One class of signal that is well known in the atmosphere is that which is phase-locked to the sun: solar tides. Because UARS views all longitudes in slightly less than one day, the Nyquist frequency corresponds to a period of 0.99 days and therefore variations with a one day period cannot be fully resolved.

With the exception of the chlorine monoxide (C1O) maps presented below, results discussed here are not expected to have a significant diurnal signal. Model calculations show that the C1O concentration has a strong dependence on solar zenith angle (SZA), although this dependence is more like a step function than a truncated sinusoid (*Froidevaux et al., 1985*). Because of this, we examine only C/O data from either the ascending or descending portion of the orbit, depending on the SZA. Since the SZA angle changes throughout the UARS month, what appear to be changes in the C1O concentration over a week or so may in fact be due partly to the change in the SZA at the viewed locations. For the results shown here, these effects are small since they occur near the polar night. One

consequence of this approach is that for *CIO*, the Nyquist period is near 2 days rather than the 1 day period obtained when both ascending and descending data are used. It is very important to realize that the *CIO* maps do not show local time variation with longitude at a given latitude,

3. TESTING AND MLS DATA PROCESSING

There are several ways to test the asynoptic mapping scheme. The initial step is to select a sampling pattern. Here we have focused on that of the UARS MLS although another UARS instrument, the Cryogenic Limb Array Etalon Spectrometer (CLAES), always views the same part of the atmosphere as the MLS and the ISAMS instrument has the capability to view the same point in the atmosphere. The mapping procedure uses Level 3AT data to determine all of the parameters of the Appendix. A slight change in the latitude bin size allows an integral number of bins to make up an orbit and it forces each bin to correspond to nearly the same latitude from orbit to orbit. The latitudes of these bins are not equally spaced, being further apart near the equator. Once missing values are filled and the coordinate rotation is performed, the FFT is determined for each bin separately. Display of the inverse transform maps requires interpolation onto a regular latitude grid. Simple tests using analytic functions as input have been used to verify that signals inside the Nyquist limits are accurately represented.

A more realistic test involves the use of a GCM to simulate the atmosphere. Model fields have been sampled at times and locations which correspond to those of the MLS sampling pattern. The resulting "data" were then used to calculate Fourier transforms ($\Psi(m, \sigma_n)$ as expressed in the Appendix). Synoptic maps were subsequently reconstructed at particular times and were compared with synoptic maps produced directly by

the model. The calculations described here used output provided by the Langley GCM (*Blackshear et al., 1988*). Figure 1 illustrates the results of such a comparison for ozone. Also included is a map obtained directly from the Level 3AT data. Because Level 3AT points are irregular in latitude and longitude, a bilinear interpolation scheme is used to produce this map. The synoptic map in Figure 1 appears to capture most of the features present in the mode], although the effects discussed earlier which are attributable to the lack of ascending/descending independence, can be seen in Fig. 1 b near the polar edge of the contours. A number of similar tests have been carried out including comparisons with other mapping techniques such as the Kalman filter. The results of these comparisons will be the subject of future publications.

Synoptic maps for O_3 , temperature (T) and water vapor (H_2O) are produced on a routine basis. *CIO* maps are produced when concentrations are elevated significantly above the noise level. Regular processing involves the calculation of Fourier coefficients for about 7.2 days (108 orbits) at all UARS pressure levels and latitude grid points. Maps are then produced for each of 7 clays at 12 GMT. The 12 hour offset of the first map from the beginning of the record is sufficient for suppression of edge effect errors as is the offset of the last map from the end of the record. Days which have large amounts of missing or corrupted data and days incorporating a yaw maneuver are omitted. Fourier coefficients are also calculated for O_3 , T and H_2O for each UARS month, allowing greater frequency resolution. Differences between maps produced from weekly and monthly runs are usually slight. Exceptions occur during intervals when the orbital period (τ_0 in the Appendix) changes more rapidly with time.

In addition to these standard products on pressure surfaces, Level 3AT data for selected days are interpolated onto constant potential temperature (θ) surfaces and used in the calculation of Fourier coefficients and maps. Such maps make it easier to display quasi-conservative features.

The Fourier transform coefficients for the sine and cosine series components are used to determine the discrete cross spectral and power spectral density functions as described by *Bendat and Piersol (1971)*. These functions are then spectrally smoothed using a Hanning window and used to find the eastward and westward propagating wave variances described by *Schäfer (1979)*. Statistical significance is determined by calculating coherency and relating it to *a posterior* probability by the procedure outlined by *Elson (1990)*.

4. RESULTS

We provide here a sampling of some of the more significant results from MLS with emphasis on evidence for transport in the polar regions during the winter and spring, Figure 2 compares Rossby-Ertel potential vorticity (PV) derived from NMC data (*Manney and Zurek, 1993*) and ClO on the 520 K θ surface for Jan. 11, 1992. This surface corresponds approximately to 46 hPa, although it can reach levels as high as about 30 hPa in the coldest part of the vortex on this day and is near the height of maximum enhanced ClO in the lower stratosphere. Although the PV is not mapped in the same way as the ClO, it is quite useful for defining the vortex, PV and ClO have substantial overlap in the sunlit region which suggests significant isolation of the air containing the ClO. The region inside the small circle is in the polar night where ClO is largely in the dimer state and not observed by MLS. *Waters et al., (1993)* discuss this in greater detail. We find that correlation between PV and chemical species is usually very good for time and space scales where both are expected to be quasi-conserved, Other examples are given below.

The synoptic maps produced from MLS observations can also be used to examine the isolation of the vortex in the SH at about 22 hPa. MLS first viewed the formation of the SH vortex in 1992. Elevated levels of ClO were detected in June and were observed to remain at a high level through mid-July at which time the platform performed a yaw

maneuver. The MLS observed the South polar region again after the next yaw on Aug. 13, when measurements showed continued high levels of ClO and diminished O_3 in the vortex. The boundary of the vortex, as delineated by the region of steep O_3 gradient, became somewhat diffuse at times, occasionally allowing low latitude air containing low O_3 mixing ratios to be drawn into the vortex, Figure 3 illustrates a 2 day sequence where high O_3 values surrounding the vortex, illustrated by the shaded region, are penetrated by several tongues of low ozone from lower latitudes, A similar pattern is noted in the PV (not shown) supporting the interpretation that large scale horizontal exchange occasionally takes place at these levels.

An examination of O_3 on the 840 K θ surface (near 10 hPa) shows this to be a very active region during the mid-winter months. In the north, a sequence of 8 days starting on Feb 21, 1993 are shown in Plates 1 and 2. It is clear that a tongue of O_3 , with high values characteristic of the equatorial regions, moves poleward. This tongue breaks off as it spirals closer to the pole. As it does, the high values seem to dissipate, consistent with diabatic downward motion in the presence of the observed negative vertical gradient in O_3 . During the final 3 days of the sequence, the polar vortex, delineated by both low ozone values and a steep gradient in PV, is offset from the pole to the side away from the high O_3 . Although the high O_3 values reach latitudes poleward of 60° there is no apparent penetration of the vortex at these altitudes.

Plate 3 shows the behavior of H_2O during the last 4 days of the sequence just described. A clear anti-correlation with O_3 is evident so that the tongue of air which spiraled in from the equatorial region has low values of H_2O . This anti-correlation is present at lower levels as well during this period. H_2O has a small positive vertical gradient so that downward motion wouldn't be expected to produce significant changes as it does for O_3 . At these levels, and for these time scales, both O_3 and H_2O should be good tracers of air motion.

Plate 4 shows temperature on the 840 K surface for these same 4 days. Since warm temperatures radiate more effectively, the distribution of temperature suggests that radiative cooling is strongest in the polar region between 150° and 210° longitude where O_3 and H_2O are high and low respectively. Since strong radiative cooling implies downward motion on an isentropic surface, the temperature distribution provides further evidence that air with high O_3 is subsiding at these longitudes in the polar region.

A similar behavior occurs in the SH during August, 1992 (not shown). Parcels of air on the 840 K surface which are rich in O_3 and poor in H_2O extend poleward from the equatorial regions, break off and spiral in towards the pole. Despite the fact that the SH is known to have a much more symmetric and much less variable vortex structure than the NH, as the ozone-rich air approaches, the vortex shifts away from the pole.

Again examining the lower levels (22 hPa), we find that as the season progresses towards spring, the anti-correlation between O_3 and H_2O remains strong. A non-axi symmetric pattern evolves as the vortex, as defined by low ozone mixing ratios, moves off the pole. The vortex begins to be eroded through stretching and breaking of large patches. An example of the SH is given in Figure 4 where low values of O_3 (shaded areas) have broken away from the main vortex remnant. This remnant has high H_2O as well. These high mixing ratios, shown as shaded regions, are also present in the large patches of air which have broken away from the vortex. The anti-correlation between O_3 and H_2O is observed, to some extent, throughout the year although it seems to be strongest when the vortex is well defined.

An examination of the Fourier coefficients is meaningful in the context of the variance of eastward and westward traveling waves and their temporal coherency. As discussed by Elson (1990), coherency represents the probability that the variance reflects a coherent signal rather than noise. This type of description is very useful for characterizing large scale, regular variations in O_3 as a function of latitude, altitude, longitudinal wavenumber

and frequency. For example, by inspecting the variance as a function of frequency, one finds that all fields exhibit a characteristic “red” spectrum, i.e. most of the variance is at low frequencies. Careful observations show that there are deviations from a smooth progression of variance with frequency and that these deviations often represent coherent waves. By contouring the variance as a function of latitude and height for a particular zonal wavenumber, the structure of the disturbance can be ascertained. An example of this is given in Figure 5 which depicts eastward propagating wavenumber 1 O_3 and T variance and probability at a period of about 8.5 days during a 38 day “month” starting on Aug. 14, 1992 (day 227). The temperature amplitude reaches values near 9 K and there is some spatial overlap between regions of large O_3 and T amplitude.

The large temperature amplitude near 5 hPa in Fig 5 suggests that maps at this altitude might show interesting structure. Fig. 6 indicates that this is indeed an active period. The two maps represent synoptic times 24 hours apart, yet temperatures have changed dramatically in some regions. The shaded area in the Antarctic region in Fig. 6b delineates temperatures above 280 K. The same area 24 hours earlier contained some temperatures closer to 250 K. *Fishbein et al.* (1993) discuss this in greater detail. During times of rapid change, such as those shown in this figure, synoptic maps produce more accurate results than time binning. The small feature at the edge of MLS observations, near the Ross Sea may be due to the lack of independence between ascending and descending nodes in the asynoptic analysis.

5. DISCUSSION AND SUMMARY

It is clear that horizontal transport can be resolved by limb observations. The transport into and out of the SH vortex examined here at 22 hPa seems somewhat limited, especially during the early and mid-winter when the vortex is strong. This is not the case

near 10 hPa where there is clear evidence of frequent poleward transport of O_3 . Although the horizontal transport does not appear to result in an exchange of air from outside the vortex to inside at this level, the descent implied at these upper altitudes could result in ozone-rich air entering the vortex at a lower level since the edge and shape of the vortex changes with altitude (*Manney and Zurek, 1993*). This process would help explain the high levels of O_3 found in the vortex in early and mid-winter { *Waters et al. (1993)*}. Horizontal transport also plays a significant role at 22 hPa during the springtime decay phase of the vortex. Additional insight into the qualitative role of non-axisymmetric horizontal and vertical transport can be gained by looking at other conserved tracer species (such as CH_4 and N_2O from CLAES).

The use of two dimensional Fourier transforms in a rotated coordinate system provides a robust approach to analyzing data provided by limb viewing instruments. One can use this technique to account for the time dependence of the observed atmosphere in a variety of useful ways. The initial MLS results presented here are mainly descriptive but quantitative studies are currently underway. Examples include the use of asymptotically mapped data for trajectory and transport calculations, the use of Fourier coefficients directly to calculate correlations between different species or between wind fields and species (to provide fluxes) and the systematic exploration of propagating variances and their spatial structures.

Figure legends

1) Orthographic projection of Northern Hemisphere O_3 in ppmv at 3.16 hPa from (a) the Langley GCM (b) the Langley GCM as observed by an instrument with the sampling characteristics of the MLS and subjected to the asymptotic mapping procedure and (c) interpolated Level 3AT data. The model day was Feb. 2 and (a) and (b) are representative

of the field at 12 GMT. The area centered on the pole without contours is not observed by the MLS.

2) (a) Potential vorticity derived from NMC data (in units of $K m^2 kg^{-1} s^{-1}$) and (b) C1O (in units of ppbv) for Jan. 11, 1992 on the 520 K θ surface. The contour spacing for C1O is .4 ppbv. The maps are centered on the North Pole and the circles enclose the polar night region.

3) Ozone (in ppmv) on the 520 K θ surface in the SH for (a) Sept. 1, 1992 (day 245) and (b) Sept. 2, 1992 (day 246),

4) Isentropic maps of (a) water vapor (ppmv) and (b) ozone (ppmv) for Nov. 6, 1991 (day 310) on the 655 K surface in the SH. High values of water vapor (> 5.5) and low values of O_3 (< 5) are shaded.

5) Height/latitude variation of (a) ozone (ppmv²) and (b) temperature (K²) variance for longitudinal wavenumber 1 and a period of 8.5 days for a 38 day period beginning Aug. 14, 1992 (day 227). Shaded regions outline areas where the probability is greater than 95%

6) Maps of SH temperature on the 4.6 hPa pressure surface for (a) Sept. 2, 1992 (day 246) and (b) Sept. 3, 1992 (day 247). The shaded region outlines areas where the temperature is greater than 280 K.

Color plate legends

Plate 1) Ozone (in ppmv) and PV for 21-24 Feb., 1993 on the 840 K potential temperature surface. Ozone levels are depicted by color values and PV by contours. PV values range from .00035 to .00045 $K m^2 kg^{-1}$.§-1.

Plate 2) As for Plate 1 but for 25-28 Feb., 1993.

Plate 3) As for Plate 2 but for H_2O (in ppmv).

Plate 4) As for Plate 2 but for temperature (K).

APPENDIX

A field, $\psi(\lambda, t, \phi, z)$, defined over longitude λ , time t , latitude ϕ and log pressure, z , can be expressed as a sum of Fourier components

$$\psi(\lambda, t) = \sum_{m=0}^M \sum_{n=0}^N \Psi(m, \sigma_n) \exp[i(m\lambda + \sigma_n t)]. \quad (A.1)$$

where $i = \sqrt{-1}$, M and N are limits to be defined, m is the longitudinal wavenumber, σ is the frequency and we have omitted the ϕ and z dependence for simplicity. The goal is to determine $\Psi(m, \sigma_n)$ and the derivation given here is based on that of *Salby*, (1982a) and *Lai/ondSfa@ord*(1988).

Central to the approach is the separation of observations into ascending and descending series denoted here by subscripts a and d . Observed longitudes and times are related to each other by

$$\lambda_{dj} = \lambda_{d0} - c_0 \tau_0 j \quad \lambda_{aj} = \lambda_{a0} - c_0 \tau_0 j \quad (\text{A.2})$$

and

$$t_{dj} = t_{d0} + \tau_0 j \quad t_{aj} = t_{a0} + \tau_0 j \quad (\text{A.3})$$

where $j = 0..J-1$, J is the total number of orbits in the reanalysis, c_0 is the zonal component of satellite speed in *rad day⁻¹*, τ_0 is the orbital period in *days*, and $\lambda_{d0}, \lambda_{a0}, t_{d0}$ and t_{a0} are the starting descending longitude, ascending longitude, descending time and ascending time for the sequence.

As shown by *Salby*, (1982a), the sub-satellite track mixes longitudes and times in a way which is not conducive to easy Fourier analysis so a new coordinate system (s, r) is defined by a rotation of (λ, t) through an angle α . This results in a similar rotation of the (m, σ) coordinate system to produce axes which we call (k_s, k_r) . The relationships between the coordinate systems are:

$$\lambda = s \cos \alpha + r \sin \alpha \quad t = -s \sin \alpha + r \cos \alpha \quad (\text{A.4})$$

$$s = \lambda \cos \alpha - t \sin \alpha \quad r = \lambda \sin \alpha + t \cos \alpha \quad (\text{A.5})$$

$$m = k_s \cos \alpha + k_r \sin \alpha \quad \sigma = -k_s \sin \alpha + k_r \cos \alpha \quad (\text{A.6})$$

$$k_s = m \cos \alpha - \sigma \sin \alpha \quad k_r = m \sin \alpha + \sigma \cos \alpha \quad (\text{A.7})$$

This rotation makes it possible to determine $\Psi(m, \sigma_n)$ by first determining $\Psi(k_s, k_r)$ using the FFT.

After this rotation, the observations for a given latitude have 2 values of r corresponding to the ascending and descending parts of the orbit. These values are denoted r_a and r_d and can be expressed as

$$r_a = \lambda_{a0} \sin a + t_{a0} \cos a = r_d - \Delta \lambda'_{ad} \sin a \quad (\text{A.8})$$

$$r_d = \lambda_{d0} \sin a + t_{d0} \cos a$$

where

$$\Delta \lambda_{ad} = \lambda_{dj} - \lambda_{aj} \Delta t_{ad} = t_{dj} - t_{aj} \Delta \lambda'_{ad} = \Delta \lambda_{ad} + c_0 \Delta t_{ad} \quad (\text{A.9})$$

Because the transformed coordinate, s decreases with j , it is desirable to reverse the series. When this is done, the $J - 1$ term becomes the first term of the series and must be accounted for as an offset when performing the Fourier transform. Therefore, using A.2, A.3 and A.5,

$$\begin{aligned} s_{dJ-1} &= (\lambda_{d0} - c_0 \tau_0 (J - 1)) \cos a - (t_{d0} + \tau_0 (J - 1)) \sin a \\ s_{dJ-1} &\approx 0 - \Delta \lambda_{ad} - c_0 \tau_0 (J - 1) \cos a - (t_{d0} - \Delta t_{ad} + \tau_0 (J - 1)) \sin a \quad (\text{A.10}) \\ &= s_{dJ-1} - \Delta \lambda'_{ad} \sin a \end{aligned}$$

As described in some detail by Salby (1982a, 1982b), Nyquist limits, which place bounds on the allowed values of k_s and k_r , can be determined. Here we denote these bounds as k_s and k_R . They are defined by

$$k_s = \pm \pi \sin \alpha / \tau_0 \quad k_R \approx \pm 1 / (2 \sin a), \quad (\text{A.11})$$

The approximate relation for k_R is due to the fact that the exact value depends on the separation between r_a and r_d . It should be noted that these rectangular limits in k_s, k_r space are not so when rotated back to m, σ space. For example, slightly higher wavenumbers (larger m) can be resolved for shorter period (larger σ) variations. Substitution of (A.11) into (A.6), and using (A.14) below, one can determine N and M in (A.1). Because m can only assume integer values, only two values of k_r are allowed for each value of k_s :

$$k_{r-} = -k_s c_0 + m\sqrt{(1+c_0^2)} \quad (\text{A.12})$$

$$k_{r+} = -k_s c_0 + (m+1)\sqrt{(1+c_0^2)}.$$

The next step is to compute the s Fourier transform of $\psi(s, r_a)$ and $\psi(s, r_d)$ and combine them with the offset terms, (A. 10) to define

$$\Psi''(k_s, r_d) = \Psi(k_s, r_d) \exp[-i(k_s s_{dJ-1} + k_{r-} r_d)] \quad (\text{A.13})$$

$$\Psi''(k_s, r_a) = \Psi(k_s, r_a) \exp[-i(k_s s_{aJ-1} + k_{r-} r_a)]$$

where $\Psi(k_s, r_a)$ is the Fourier transform of $\psi(s, r_a)$ and $\Psi(k_s, r_d)$ is the Fourier transform of $\psi(s, r_d)$. From A. 11, k_s takes on the values

$$k_s = 2\pi j \sin \alpha / (J\tau_0) \quad j = -J/2, -J/2 + 1 \dots J/2 \quad (\text{A.14})$$

The final step is to express the s and r Fourier transform, $\Psi(k_s, k_r)$ in terms of $\Psi''(k_s, r_d)$ and $\Psi''(k_s, r_a)$. Recalling that there are only two values of k_r for each k_s , we arrive at

$$\Psi(k_s, k_{r-}) = [\Psi''(k_s, r_a) - \Psi''(k_s, r_d) \exp(-i\Delta\lambda'_{dd})] / [1 - \exp(-i\Delta\lambda'_{dd})] \quad (\text{A.15})$$

$$\Psi(k_s, k_{r+}) = [\Psi''(k_s, r_a) - \Psi''(k_s, r_d) \exp(-ir_d / \sin \alpha)] / [1 - \exp(-i\Delta\lambda'_{dd})]$$

Each value of $\Psi(k_s, k_r)$ corresponds to a particular value of $\Psi(m, \sigma_n)$ so that the inverse transform, (A.1) is actually carried out over allowable (m, σ_n) pairs.

Acknowledgements. The authors thank the UARSProject, J. Waters and the MLS Team for providing support, G. L. Manney for supplying PV and Dr. W. Grose for supplying model data. This research was performed at the Jet Propulsion Laboratory, California

Institute of Technology under contract with NASA. Some of the computations performed in support of this work were carried out on the JPL Cray Y-MP.

REFERENCES

- Blackshear, W. T., W. L. Grose and R. E. Turner, Simulating sudden stratospheric warming synoptic evolution. *Quart. J. Roy. Met. Soc.*, **113**, 815-846, 1987.
- Benndat, J. S. and A. G. Piersol, *Random data: Analysis and measurement procedures*. Wiley-Interscience, New York, 1971.
- Elson, L. S., Satellite observations of instability in the middle atmosphere. *J. Atmos. Sci.*, **47**, 1065-1074, 1990.
- Fishbein, E. F., L. S. Elson, L. Froidevaux, G. L. Manney, W. G. Read, J. W. Waters, and R. W. Zurek, MLS observations of stratospheric waves in temperature and O_3 during the 1992 southern winter, *Geophys. Res. Lett.* in press, 1993.
- Froidevaux, L., M. Allen and Y. L. Yung, A critical analysis of ClO and O_3 in the mid-latitude stratosphere. *J. Geophys. Res.*, **90**, 12999-13030, 1985.
- Haggard, K. V., E. E. Remsberg, W. L. Grose, J. M. Russell III, B. T. Marshall and G. Lingenfelter, Description of data on the Nimbus 71.1 MS Map Archival Tape. Temperature and geopotential height. *NASA Tech. Paper 2.55.?*, 1986.

- Isit, L. R. and J. L. Stanford, Applications of asynoptic space- time Fourier transform methods to scanning satellite measurements. *J. Atmos. Sci.*, 45, 3784-3799, 1988.
- Manney, G. L. and R. W. Zurek, Interhemispheric comparison of the development of the stratospheric polar vortex during fall: A 3- dimensional perspective for 1991-1992. *Geophys. Res. Lett.*, in press, 1993.
- Reber, C. A., The Upper Atmosphere "Research Satellite. *EOS Transactions, American Geophysical Union*, 71, 1867-1878, 1990.
- Salby, M. L., Sampling theory for asynoptic satellite observations, Part 1: Space-time spectra, resolution and aliasing. *J. Atmos. Sci.*, 39, 2577-2600, 1982a.
- Sal by, M. L., Sampling theory for asynoptic satellite observations. Part 11: Fast Fourier synoptic mapping. *J. Atmos. Sci.*, 39, 2601-2614, 1982b.
- Waters, J. W., L. Froidevaux, W. G. Read, G. L. Manney, L. S. Elson, D. A. Flower and R. F. Jarnot, Stratospheric Chlorine Monoxide and Ozone in the 1991-92 Northern Hemisphere Winter. *Nature* .262, 597-602, 1993.

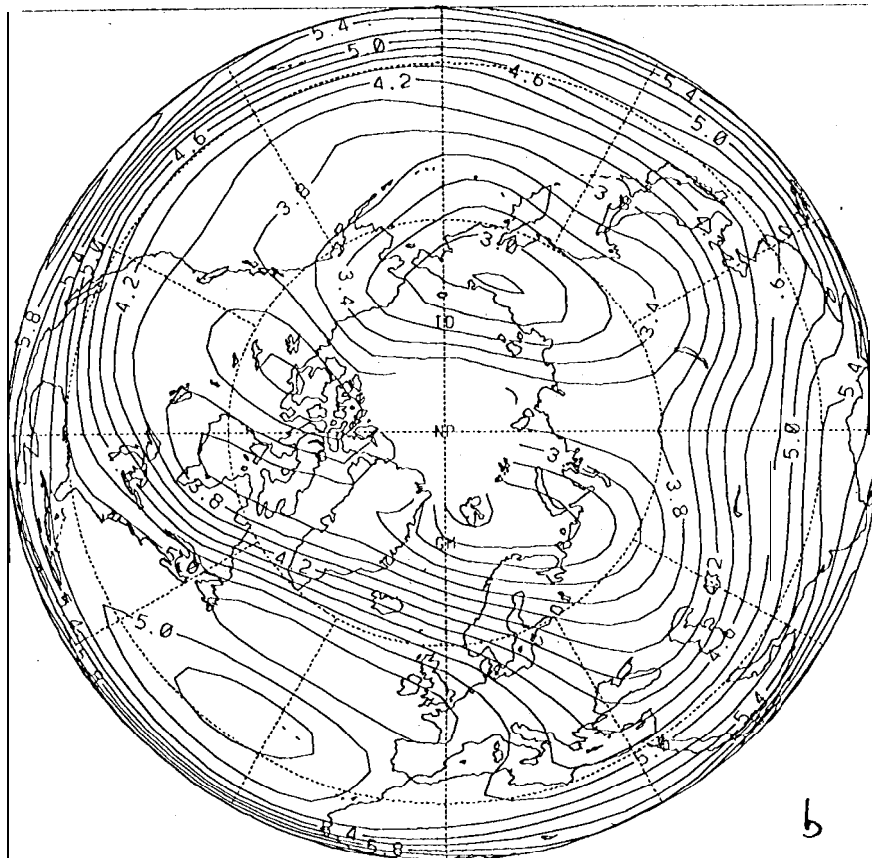
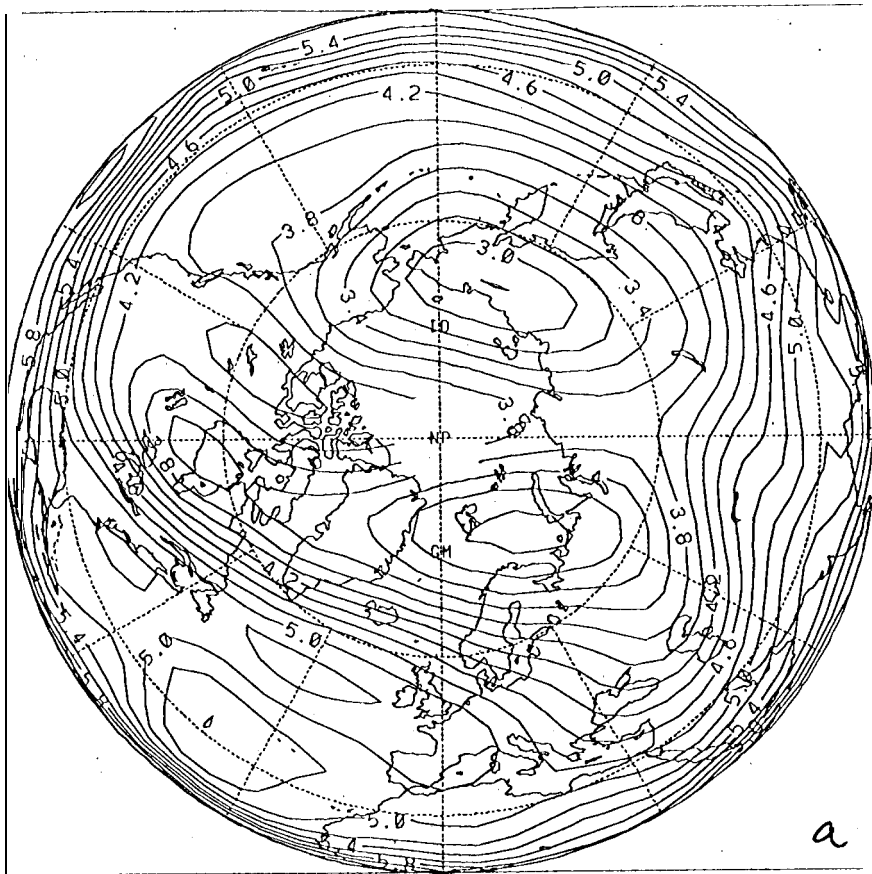


Fig 1



CONTOUR FROM 3 TO 6 BY .2

C

Fig 1

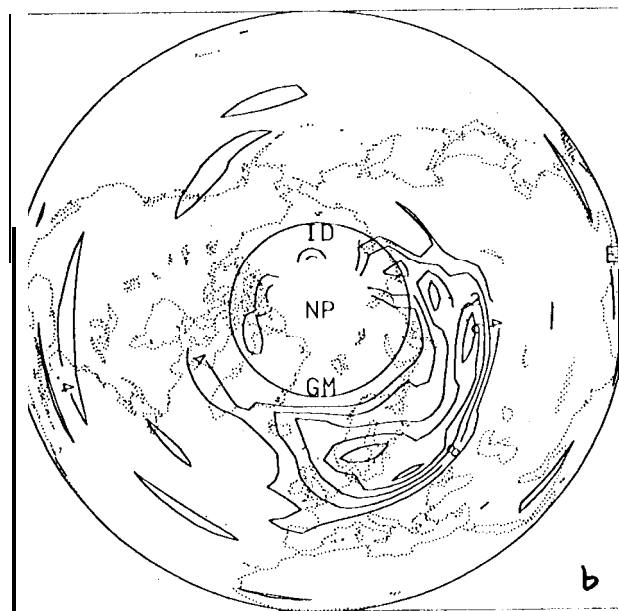
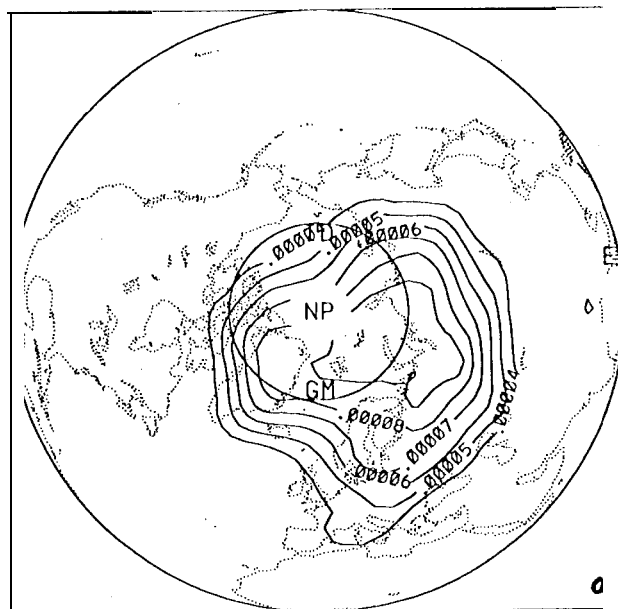


Fig 2

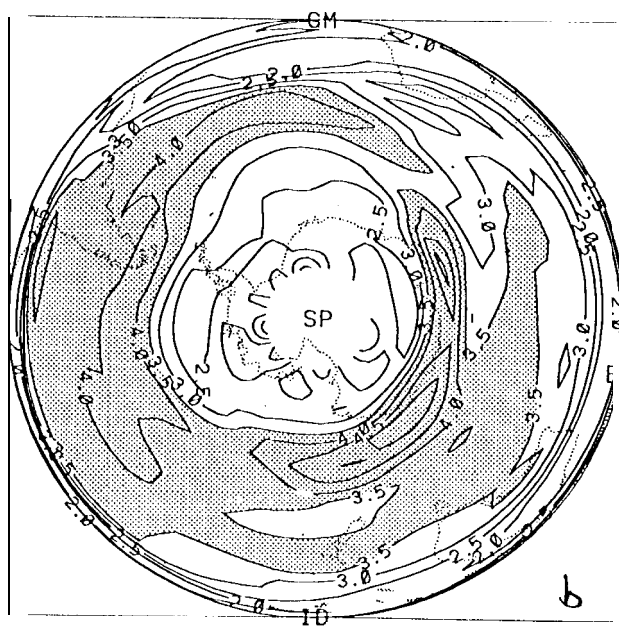
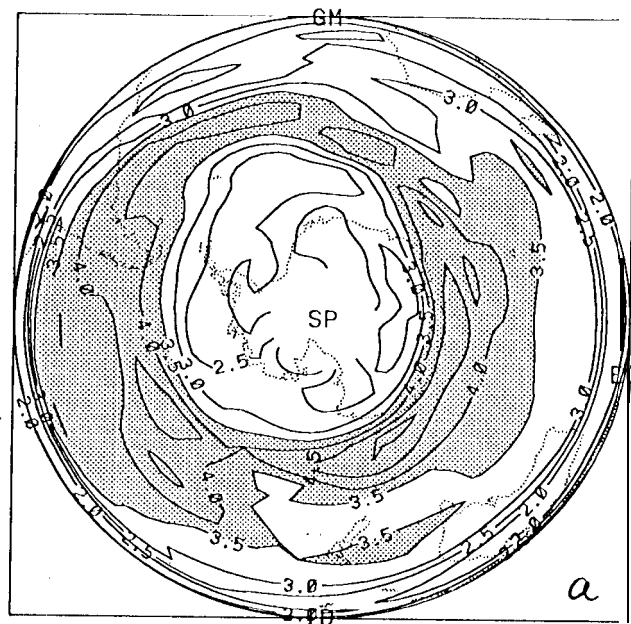


Fig 3

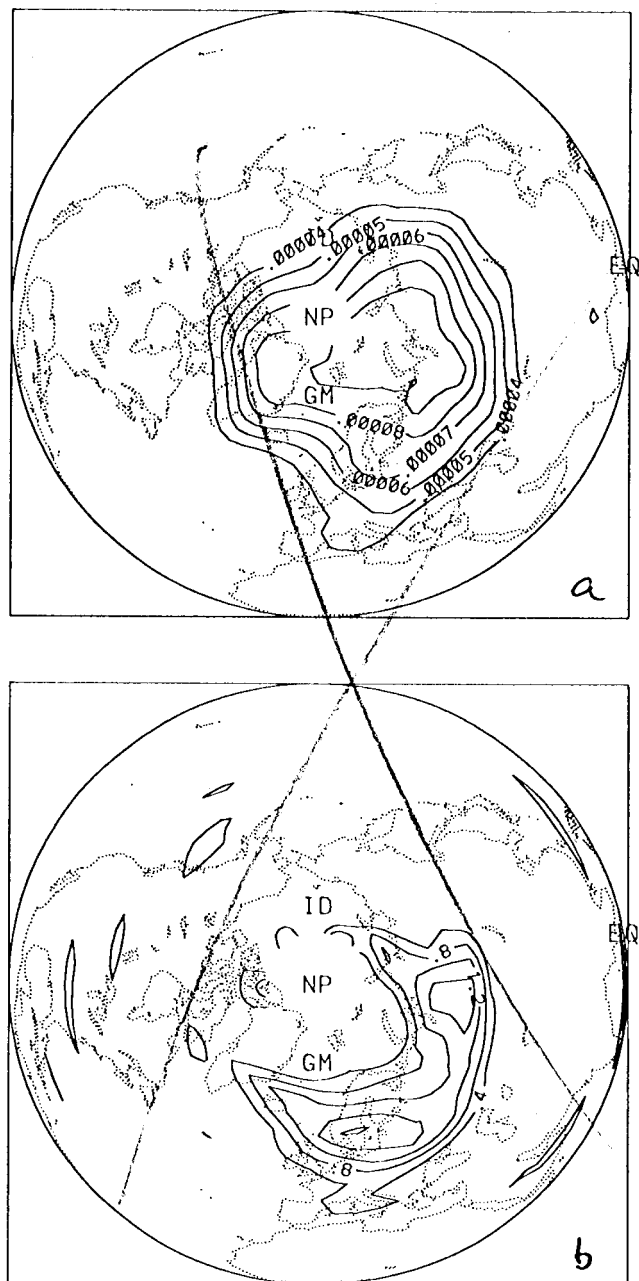


Fig 2

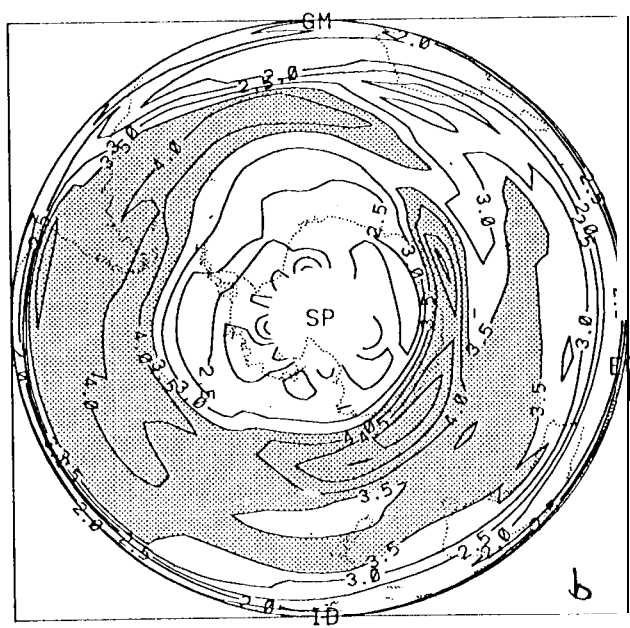
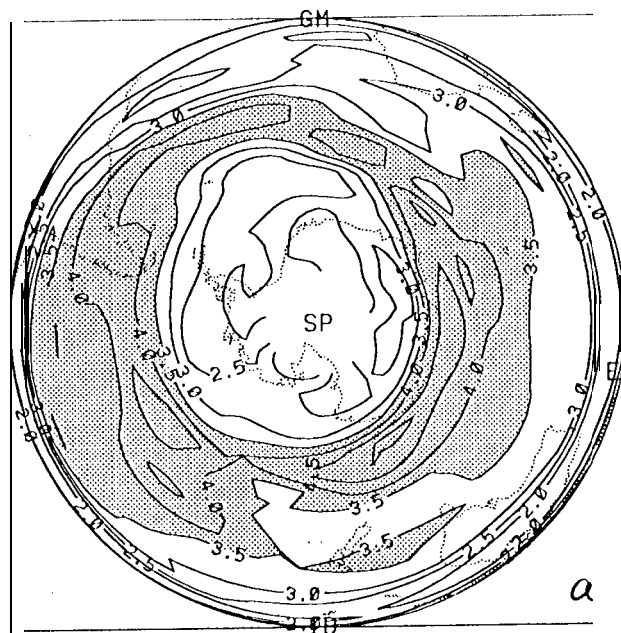


Fig 3

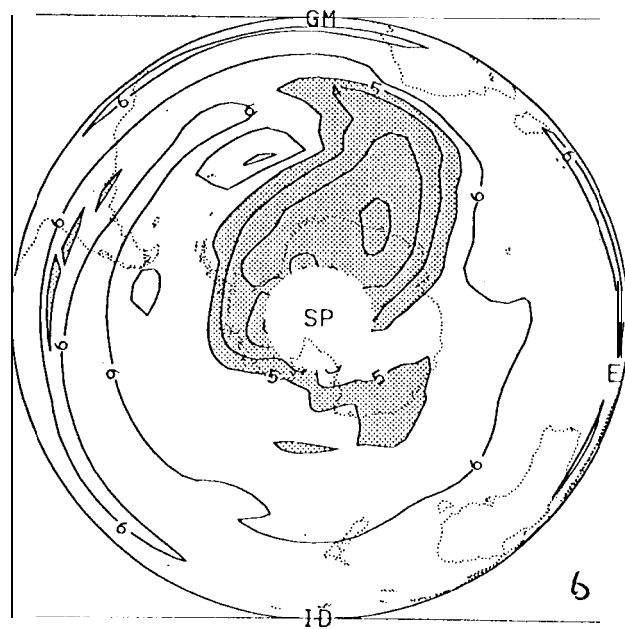
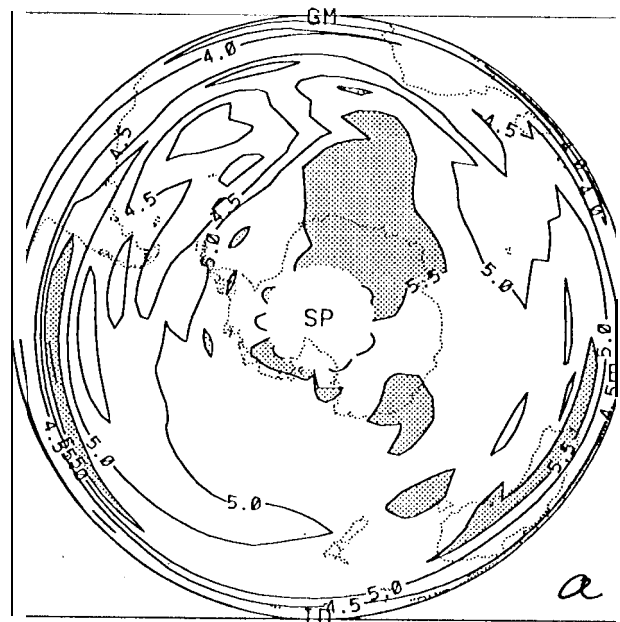


Fig 4

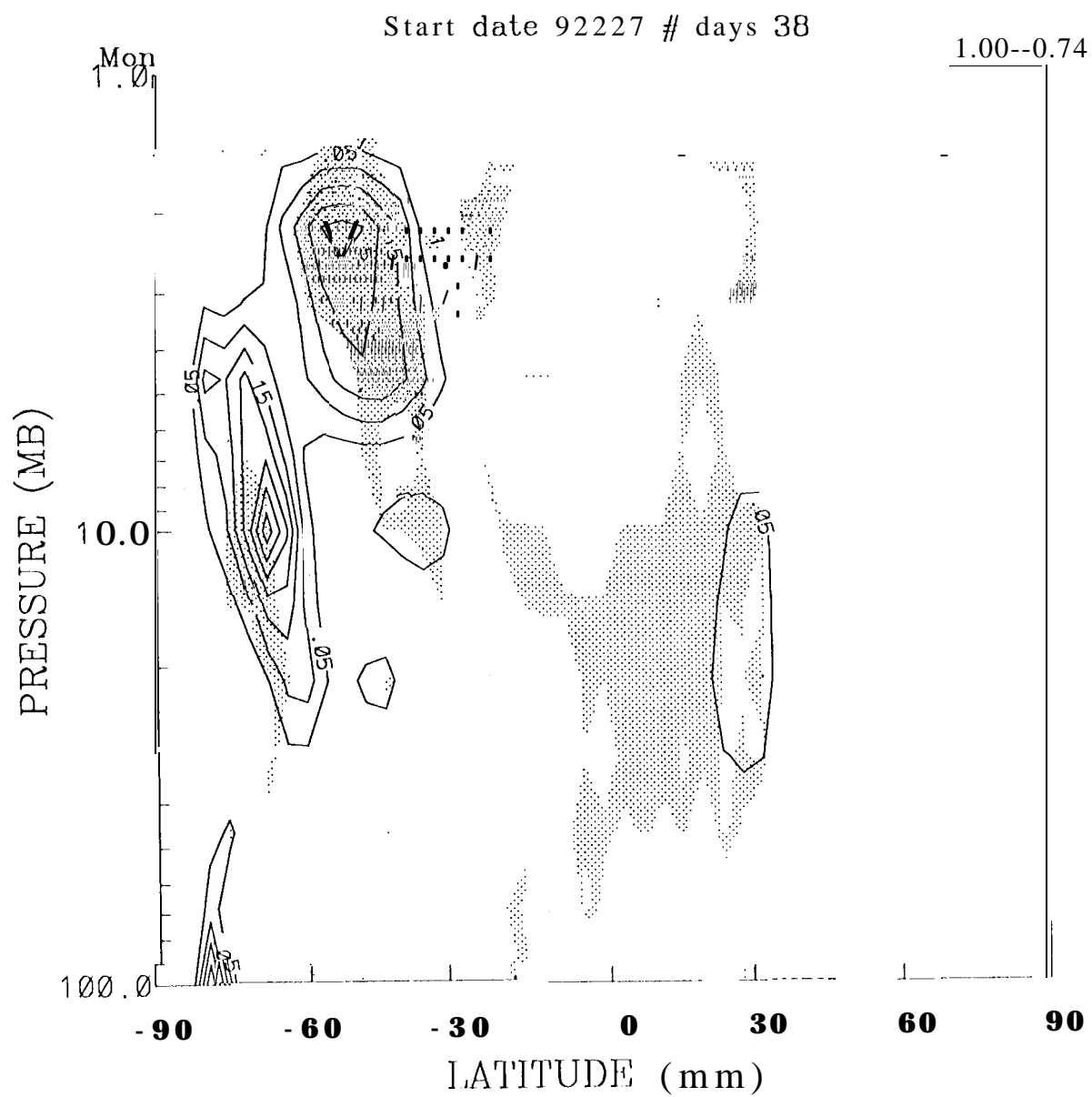


Fig 5a

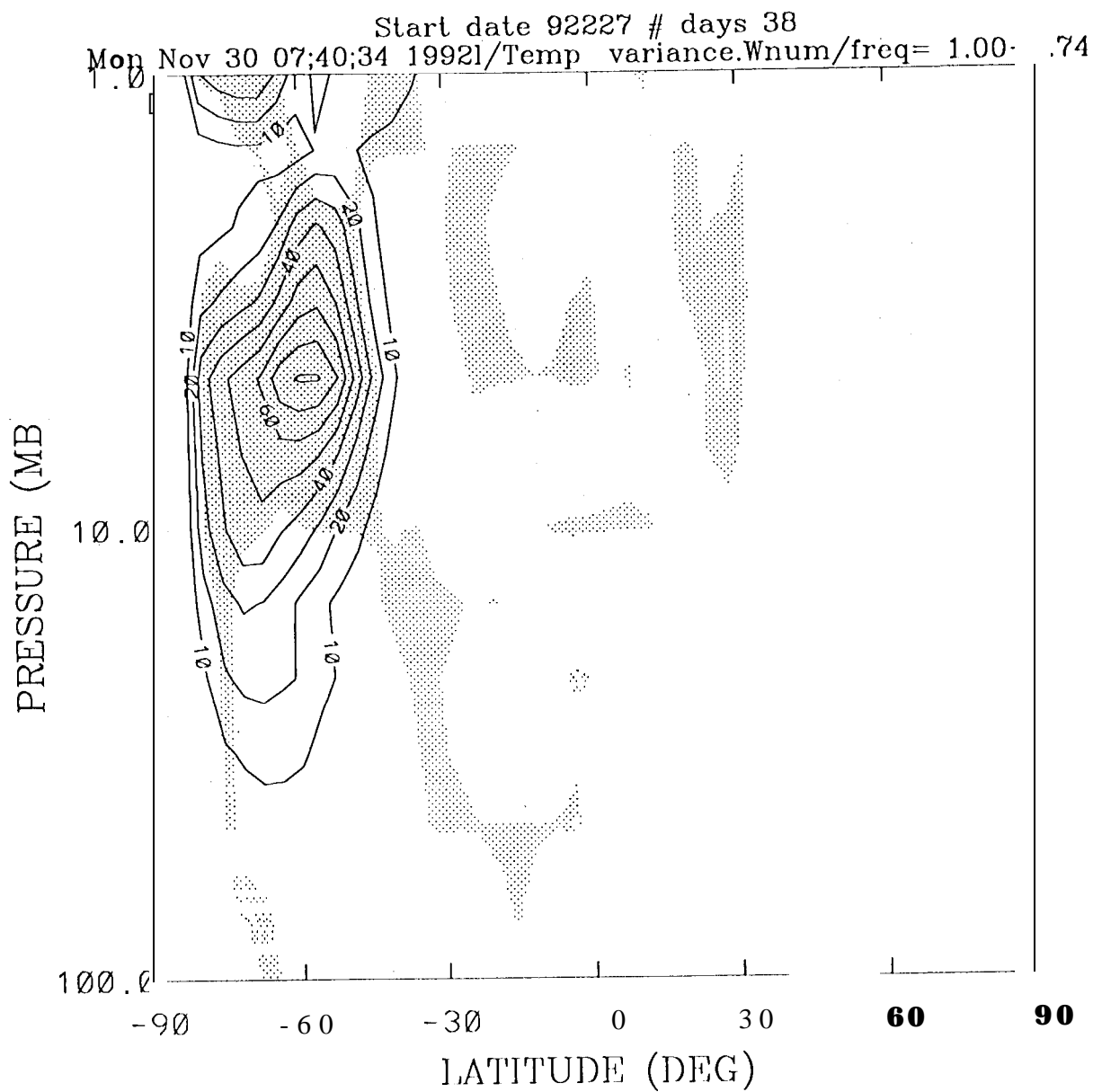


Fig 5b

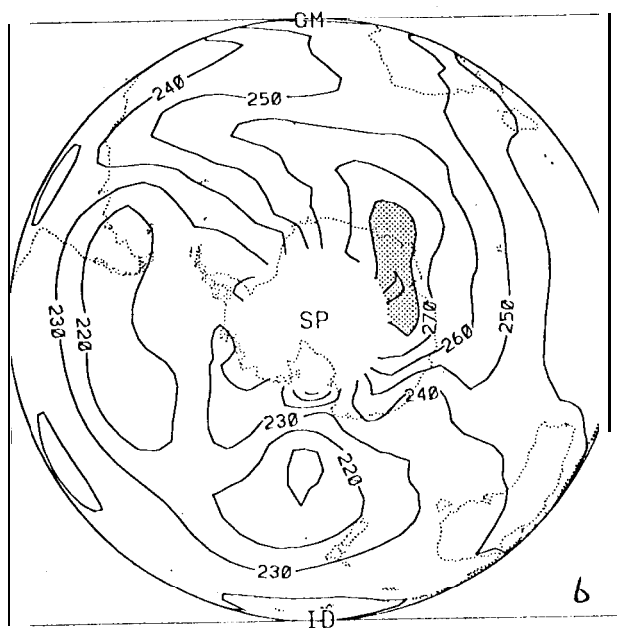
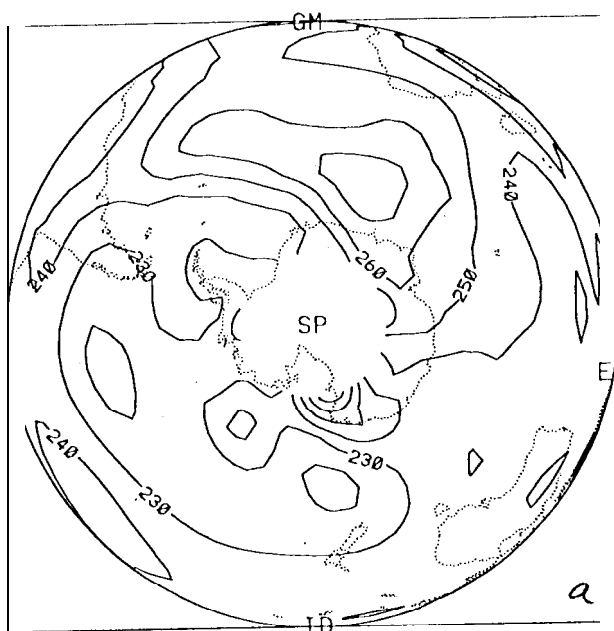
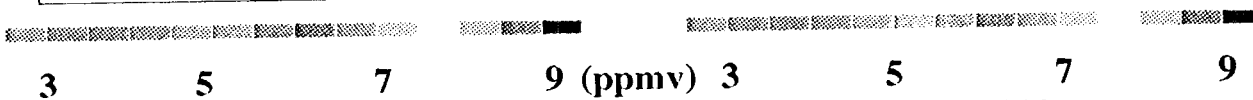
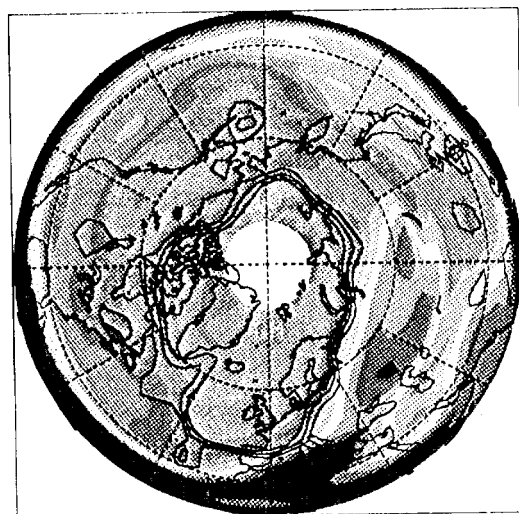
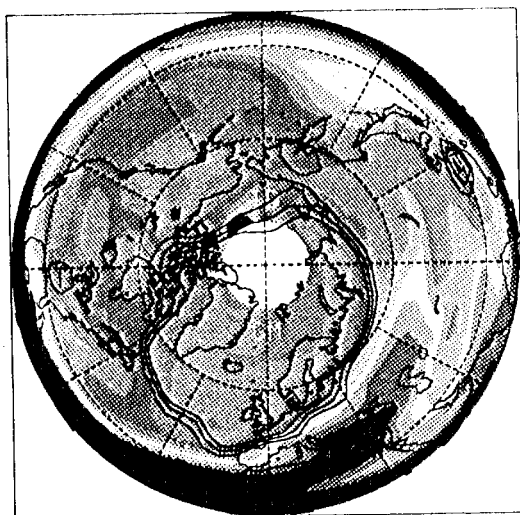


Fig 6

Feb 21, 1993

OZONE

Feb 22, 1993



Feb 23, 1993

Feb 24, 1993

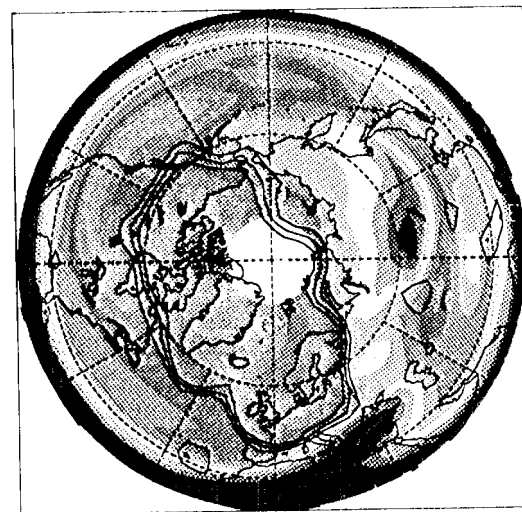
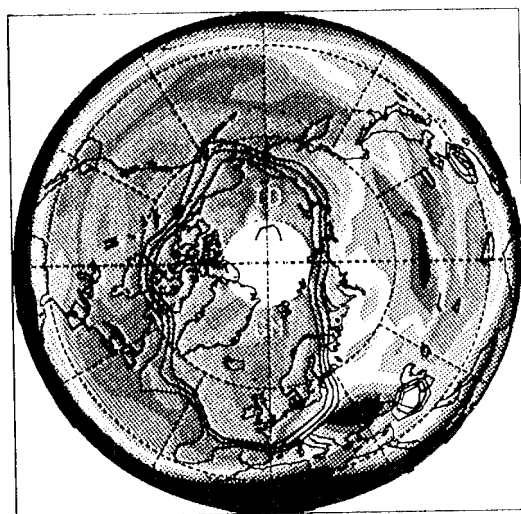
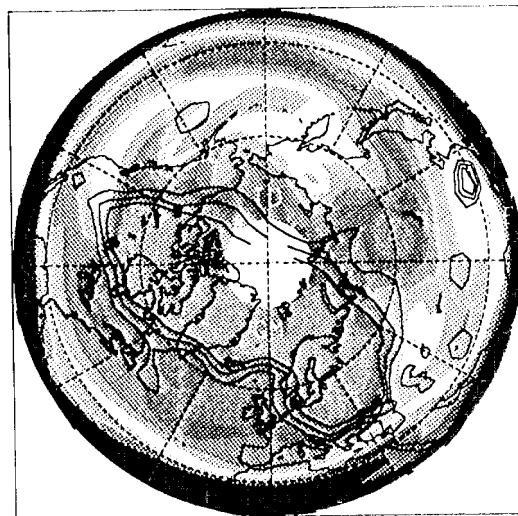
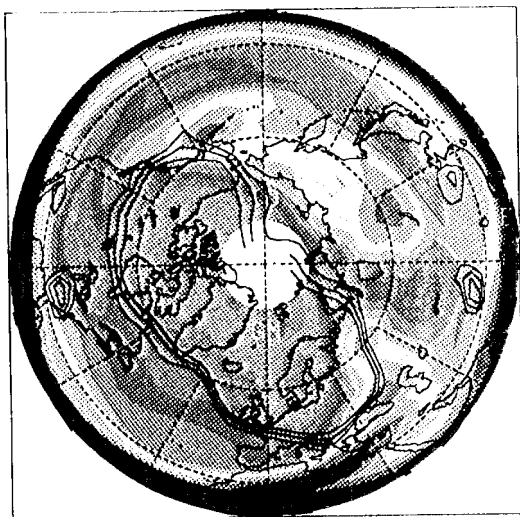


Plate 1

Feb 25, 1993

OZONE

Feb 26, 1993



3

5

7

9 (ppmv)

3

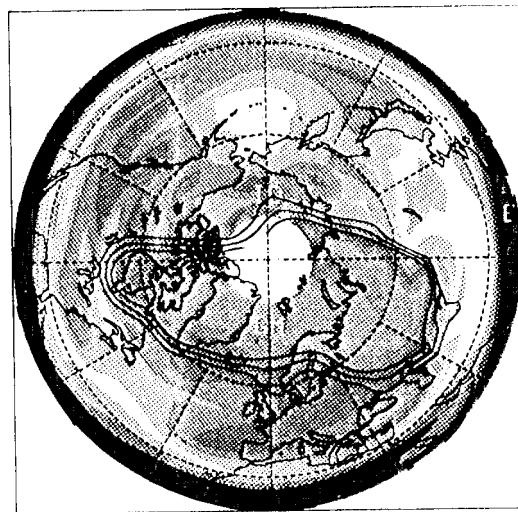
5

7

9

Feb 27, 1993

Feb 28, 1993



3

5

7

9

3

5

7

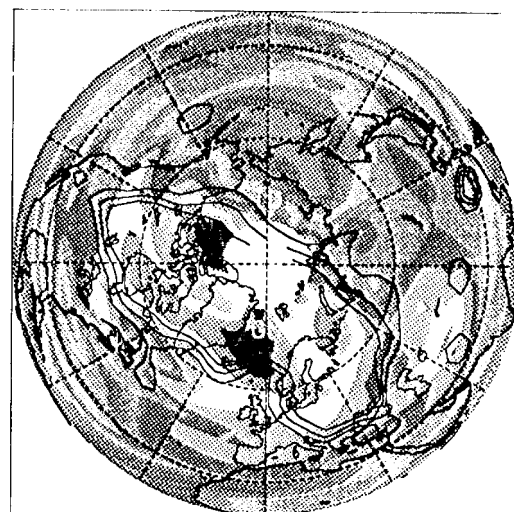
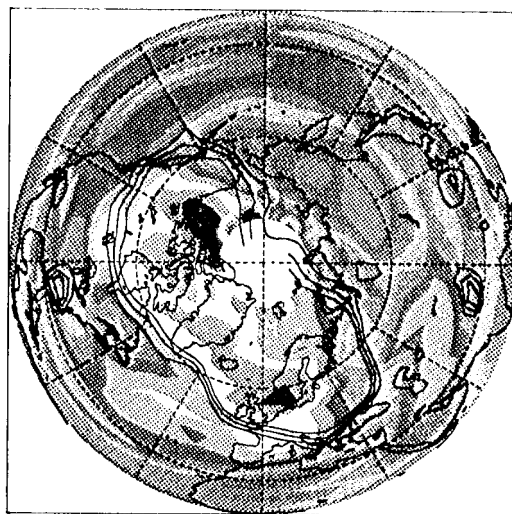
9

Plate 2

Feb 25, 1993

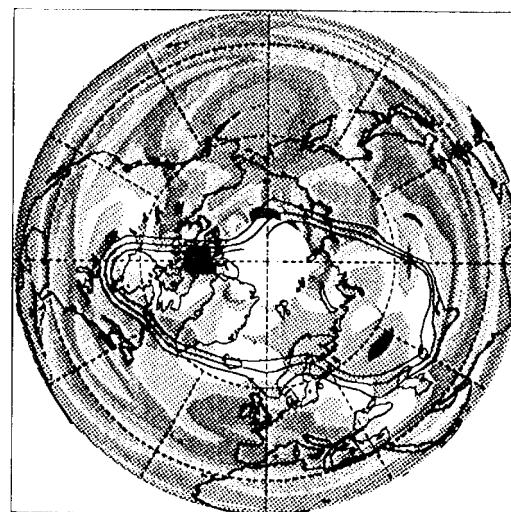
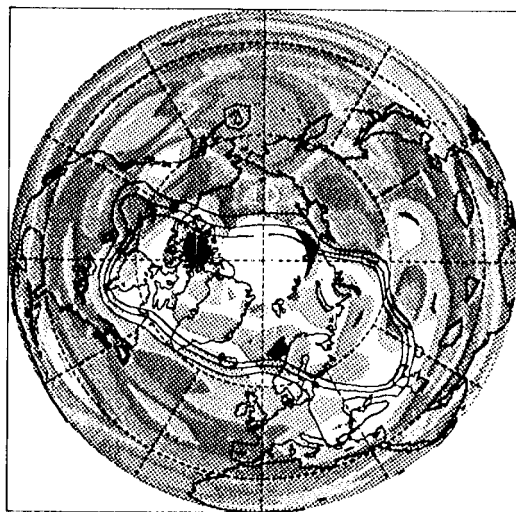
WATER

Feb 26, 1993



5 6 (ppmv)
Feb 27, 1993

5 6
Feb 28, 1993



5 6

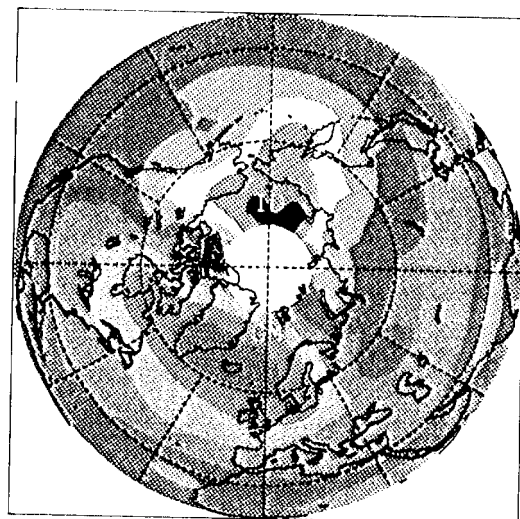
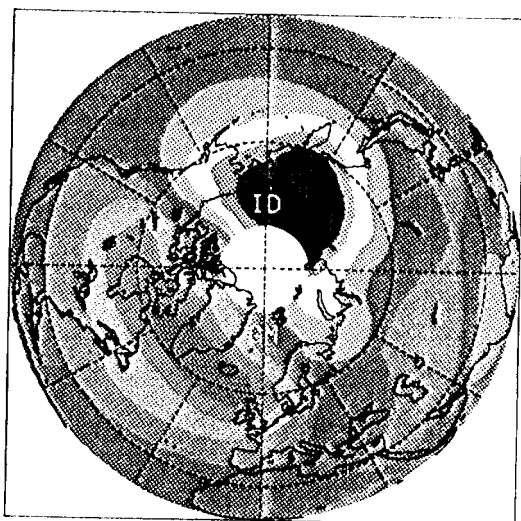
5 6

Plate 3

Feb 25, 1993

TEMPERATURE

Feb 26, 1993



205

225

245

K

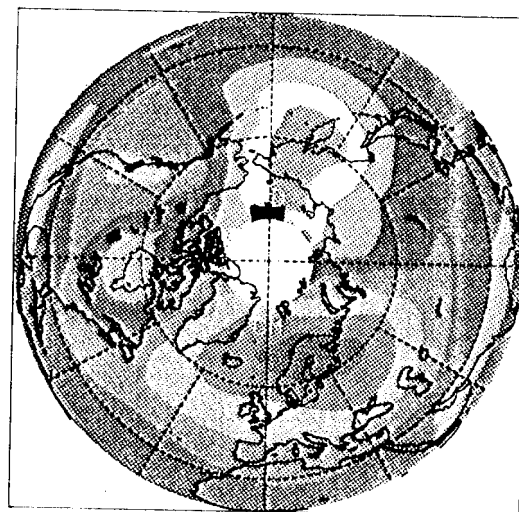
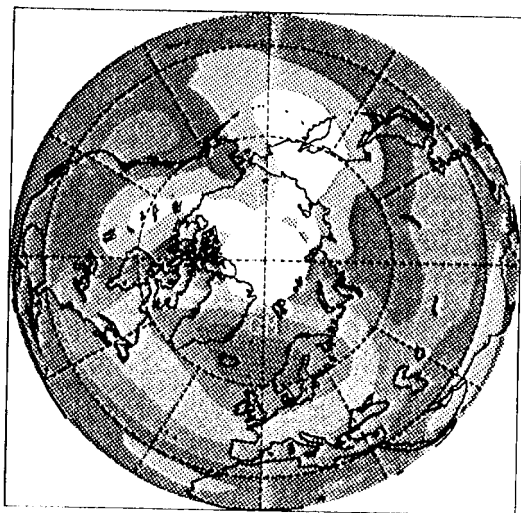
205

225

245

Feb 27, 1993

Feb 28, 1993



205

225

245

205

225

245